Platinum Nanometal Interconnection of Copper-Carbon Nanotube Hybrid Electrical Conductors

Anthony P. Leggiero[a,b]*; Shannon D. Driess*[b,c]*; Erin D. Loughran*[b,c]*; Dylan J. McIntyre*[a,b]*; Richard K. Hailstone*[d]*; Cory D. Cress*[f]*; Ivan Puchades*[b,e]*; Brian J. Landi*[b,c*]

[a]Department of Microsystems Engineering, [b]NanoPower Research Laboratories, [c]Department of Chemical Engineering, [d]Center for Imaging Science, and [e]Department of Electrical and Microelectronic Engineering, Rochester Institute of Technology, Rochester, New York 14623, United States

[f]Electronics Science and Technology Division, United States Naval Research Laboratory, Washington, District of Columbia 20375, United States

***Corresponding Author**

Tel: 585-475-4726

Email: brian.landi@rit.edu

ABSTRACT

This study demonstrates the versatility of Joule heating driven chemical vapor deposition to deposit nanometal interconnections into porous CNT roving with application in the production of high electrical conductivity copper-carbon nanotube (Cu-CNT) hybrids. Modifications of vapor deposition parameters allow for deposited nanometal masses from less than 5 % w/w to over 85 % w/w and distributions that can be controlled towards either hot-spot site-specificity or overall uniformity. Depositions of copper, platinum, nickel, palladium, ruthenium, rhodium, and iridium are demonstrated from acetylacetonate precursors. In particular, platinum acetylacetonate ($Pt(acac)_2$) deposits nanometal seeds that adhere tightly to the CNT roving, producing improvements in resistance and specific conductivity. The properties of the platinum deposition compared to the copper deposition motivate an investigation into its use as an interfacial layer for Cu-CNT hybrids. CNT conductors with ~30 % w/w platinum are electroplated with copper, densified, and annealed to produce Cu-CNT hybrid conductors with specific conductivities as high as 5772 $S \cdot m^2/kg$ and TCR (from 300–600 K) as low as $3.12 \times 10^{-3}\ K^{-1}$, indicating good interconnection of the metal and CNT portions. Room temperature conductivities of 29.8 MS/m are achieved, comparable to metallic conductors. Thus, $Pt(acac)_2$ seeded Cu-CNT hybrids offer abundant promise in high conductivity applications.

KEYWORDS

Carbon nanotube; composite conductors; hybrid conductors; chemical vapor deposition; platinum nanometal; Cu-CNT; integrated hybrids

TEXT

1. Introduction

Metal-carbon nanotube hybrids are a promising approach to combine the advantages of both materials into a single composite electrical conductor. Conventional metals such as copper offer high electrical conductivity (58 MS/m) around room temperature, but decline in operation at elevated temperatures due to a high temperature coefficient of resistance (TCR) (3.83×10^{-3} K^{-1} with respect to 300 K) [1]. For example, the conductivity of copper decreases by a third from 300 K to 450 K. Conversely, bulk carbon nanotube (CNT) conductors offer a combination of a low TCR [2–4] and robust mechanical properties (i.e. high tensile strength, flexibility, and corrosion resistance) [5,6], but have an order of magnitude lower room temperature electrical conductivity compared to both common conductor metals like copper of 58 MS/m [1] and the theoretical limit for individual CNTs of >100 MS/m [7,8]. Thus, a hybrid material that is able to combine the high electrical conductivity of a metal like copper with the low TCR of CNTs promises to reduce ohmic losses in higher temperature applications such as in transformers, generators, and motor stator windings [6].

There have been a number of studies in the production of metal-CNT hybrid electrical conductors through techniques such as electroplating [2,9–13], powder processing [14–17], and physical vapor deposition [18–21]. The approach using CVD to deposit metals onto CNTs has emerged as a novel alternative compared to these other techniques described recently in a comprehensive review [22]. The initial study to demonstrate Joule heating driven CVD of a bis(t-butylacetoacetato) Cu(II) [$Cu(tBAOAC)_2$] precursor towards the purpose of producing bulk Cu-CNT electrical conductors established a number of distinct advantages conferred by the technique [23]. Modification of the applied current to heat the CNT substrate conductor allows depositions to be specifically targeted towards hotter regions in the conductor. These regions can naturally

exist near areas of high resistance. Furthermore, the use of a penetrating vapor allows for the deposition of metal throughout the interior volume of the CNT substrate conductor, in contrast to the surface depositions of physical vapor deposition and certain demonstrations of aqueous electroplating. Thus, the potential exists for nanometal depositions that are able to bridge areas of high resistance and form interconnections both between discrete bundles of CNTs and between CNTs and metal overcoats, thereby enabling enhanced electrical transport throughout the composite. Finally, Joule heating driven CVD can be carried out within the period of an hour or less, a substantial improvement over the up to 24 hour period that metal seeding via electroplating in an organic solution may take [24]. The nanometal deposits formed during CVD processing may then act as nucleation sites or "seeds" for subsequent electroplated coating [23].

While the initial study [23] focused on copper seeds deposited from the $Cu(tBAOAC)_2$ precursor, many metal-organic precursors are available making it possible to use the technique to deposit a wide variety of metals with little to no change in deposition conditions. The high contact angle of spherical copper seed particles indicates limited physical and electrical interaction between the metal and CNTs, a phenomenon that has been frequently identified in the literature [13,22,25,26]. Attempts to improve electrical transport across the copper-CNT interface typically involve the functionalization of the CNT surface [12,13,22,27], or the use of an interfacial metal [11,13,17,22,28]. In the latter case, the ideal choice for the interfacial metal deposited through the CVD technique would result in seeds that act both as anchor points for the electroplating of copper and as electrical interconnection sites in their own right. Computational studies have indicated that metals like titanium, platinum, and palladium should have improved contact resistance [29] and stronger binding energies [30,31] with CNTs compared to copper and other common electrical conductors like gold. A previous study of a titanium adhesion layer deposited through thermal

evaporation demonstrated that such metal adhesion layers can also improve the temperature stability of a copper overcoat [32]. Additionally, previous literature demonstrated that platinum and palladium seem to interface well with bulk CNT wires, allowing for the maintenance of a low TCR with improved conductivity in metal plated CNT wires [2]. However, there have not been investigations into the use of metal like platinum, palladium, and related metals as interfacial or seeding layers for copper-CNT composites.

In this study, we demonstrate the Joule heating driven CVD of platinum, palladium, nickel, ruthenium, rhodium, and iridium in comparison to the baseline copper seeds. The acetylacetonate (acac) versions of each precursor are utilized to produce the depositions, since the thermal decomposition of this family of precursors have been extensively studied [33–35]. The acetylacetonate precursors decompose at elevated temperatures with the typical evolution of acetylacetone and related decomposition products [34], leaving behind metal films. $Cu(acac)_2$ and $Pt(acac)_2$ in particular have both been observed to decompose in the range of 225–250°C [35,36]. To produce the highest quality hybrid electrical conductors, the impact of the mass and morphology of the seeds deposited via CVD must be investigated. In this work, we explore in depth the effects of precursor temperature, deposition pressure, the interval and intensity of the applied heating current, and the effect of precursor mass on the deposited nanometal mass and morphology. We demonstrate that platinum nanometal seeds deposited from platinum acetylacetonate [$Pt(acac)_2$] fulfill the criteria of an effective interfacial interconnection metal, lowering the resistance while increasing specific conductivity of nanometal seeded composites. After electrodeposition of copper, densification, and annealing, the $Pt(acac)_2$ seeded Cu-CNT hybrids are measured to produce combinations of high specific conductivity and low TCR that

indicate good electrical interconnection of the conductors, with conductivities approaching those of traditional metals.

2. Experimental

All depositions described herein are carried out onto a commercial CNT roving from Nanocomp Technologies Inc. (a Huntsman Company) (Miralon® lot 954738). CNT roving is an unspun free-standing textile comprising CNT bundles that is ribbon-like in form, with average cross-sectional dimensions of 30 μm × 1.53 mm (with 20 % deviation possible in either dimension) [32], an average density of 0.12 g/cm^3 [23], and linear density of 9.24 ± 0.35 mg/m when vacuum dried. Optical and scanning electron microscopy (SEM) images of the material are presented in Fig. S1. The surface clearly displays the CNT bundle structure, with no visible particles or impurities. The backscatter electron (BSE) image of the region shown in Fig. S4b has very low contrast, indicating a generally homogenous atomic composition. Energy dispersive x-ray spectroscopy (EDS) presented in Fig. S4g shows a strong carbon signal with a smaller peaks for iron (from the residual synthesis catalyst), as well as minor sulfur, silicon, and aluminum impurity peaks. The average resistance per length (R/L) of the dried material is 354 ± 12 Ω/m. A mechanical analysis of this material can be found in previously published work [23,32].

Joule heating driven CVD was carried out in a three-neck flask, outlined in Fig. S2 and described in our previous study [23]. In this setup, copper electrical leads crimped to flat copper clips are passed through rubber septa on opposite ends of the flask. Three 12 cm strands of roving are suspended in parallel between the flat copper clips. The strands of roving shared a common point of contact at the clips but otherwise hang free from one another within the flask. Under an inert argon atmosphere within a glovebox, masses of 5 mg to 50 mg precursor are added to the bottom of the flask. The precursors utilized are copper (II) acetylacetonate (CAS #13395-16-9,

Sigma-Aldrich 99.9%), platinum (II) acetylacetonate (CAS #15170-57-7, STREM 98%), nickel (II) acetylacetonate (CAS #3262-82-2, Sigma-Aldrich 95%), palladium (II) acetylacetonate (CAS #14024-61-4, STREM 99%), ruthenium (III) acetylacetonate (CAS #14284-93-6, STREM 99%), rhodium (III) acetylacetonate (CAS #14284-92-5, STREM 97+%), and iridium (III) acetylacetonate (CAS # 15635-87-7, Alfa Aesar Ir 37.5% min). A hose-barb adapter with a stopcock is used to seal the center neck of the flask. After removing the flask from the glovebox, the center neck is connected to a Schlenk line, which may provide either vacuum or 5 % H_2/95 % Ar (mol/mol) gas. The flask is cycled between vacuum and the reducing gas three times before pumping down to a target pressure of 166 Torr, 0.300 Torr, or 0.175 Torr. A heating mantle is used to sublimate the precursor from the bottom of the flask, and the flask is wrapped in insulating glass wool for more even heating. Precursor temperature is modified by regulating the temperature of the heating mantle to set points between 130°C to 210°C.

As described in previous work [23], deposition is carried out through the application of current to the CNT roving to induce Joule heating, as shown in Fig. S3. This Joule heating produces the thermal energy required to decompose the metal-organic precursor into metal on contact with the CNTs. Two variations of the deposition process are presented in this text. In the continuous filament heating CVD (CFH-CVD) process, current is applied to the CNT roving continuously throughout the entire one hour deposition process. The vapor phase precursor decomposes immediately upon contact with the hot CNT roving. In the delayed filament heating CVD (DFH-CVD) process, no electrical bias is initially applied to the CNT roving, and the vapor precursor is allowed to condense onto the cool (unheated) CNT surface for a one hour period. After the one hour condensation of the precursor, 5 % H_2/95 % Ar gas is introduced into the flask to return it to atmospheric pressure and then current is applied for a period of five minutes to

decompose the condensed metal-organic precursor. In either process, the total current applied to the three roving strands was set to values between 0.45 A to 1.2 A (between 150 mA/roving and 400 mA/roving). At applied currents of 400 mA/roving and above, samples of the CNT roving are not consistently stable and sometimes fail due to excessive current induced heating [37] over the deposition period.

Electroplating was carried out in the "sandwich" cell configuration described previously [23]. Briefly, the CVD seeded CNT roving is placed between a folded piece of Whatman 42 filter paper to act as a separator. Strips of battery grade copper foil are placed on either side of the filter paper as an anode. The cell stack is then placed between two glass slides and wrapped in Kapton tape to provide even compression. This cell is then submerged in the copper electroplating solution (Transene Acid Copper) and hooked up to a power source (Arbin BT2000). Plating is carried out under constant-current conditions of 7.6 A/g to 15 A/g applied for time between 50 minutes and 3 hours to reach a similar final total metal mass of 94.5 ± 0.2 %. Here, plating rate has been presented based on the mass of the CNT roving (A/g) rather than its surface area (A/cm^2) due to local variations in the material's surface area. After electroplating, the hybrid electrical conductors were densified in a rolling mill then annealed at 300°C for 3 hours in 5% H_2/95% Ar (mol/mol) gas as described previously.[23]

A Mettler Toledo XP-2U microbalance was used to measure sample mass. Sample lengths were determined using Marathon CO030150 high precision digital calipers. Electrical resistance was measured through a room temperature current-voltage (IV) sweep up to 50 mA for CVD seeded samples or 100 mA for electroplated and finished conductors in a four-point probe configuration with a National Instruments NI PXI-4110 programmable power supply and PXI-4072 digital multimeter. The temperature coefficient of resistance (TCR) was measured using a Janis VPF-800

cryostat attached to a National Instruments NI PXI-4110 programmable power supply and an NI PXI-4072 digital multimeter. Resistance was measured through an IV sweep up to 100 mA in a four-point probe configuration at a base pressure of 10^{-6} mBar from 300 K to 600 K (26.85°C to 326.85°C) with an interval of 5 K. Two temperature cycles were measured for each sample and the data presented is from the second cycle which eliminates the effects of high temperature annealing and atmospheric doping [38,39] from the measurements. TCR was determined from the average slope of the resistance relative to the value measured at 300 K with respect to temperature. A FLIR A35 IR camera was used to obtain thermal images of the CNT roving as a function of electrical bias in air. An emissivity correction of 0.825 (determined through ASTM E1933) was applied to the thermal measurements of the CNT roving. The nanoscale morphology in the hybrid CNT conductors was evaluated by Hitachi S900 and Hitachi S4000 SEMs. Secondary electron micrographs were taken with accelerating voltages of 2-10 keV. Cross-sections for electrical conductivity calculations were produced by sectioning the conductor with a razorblade. EDS and BSE imaging were carried out in a Tescan Mira3 SEM equipped with a Bruker XFlash 6|30 EDS. Electron micrograph and EDS data were acquired with an accelerating voltage of 20 keV. Cross-sections for EDS were produced by setting the samples in epoxy, cross sectioning with an ultramicrotome, and then coating the exposed sample surface with about 15 nm of conductive carbon.

3. Results and Discussion

3.1. Chemical Vapor Deposition of Nanometal Seeds

In a prototypical study, copper and platinum were deposited from 25 mg of their respective acetylacetonate forms in a one hour DFH-CVD at 166 Torr with an applied current of

350 mA/roving and a mantle temperature of 200°C. Under scanning electron microscopy (SEM), shown in Fig. 1a, the deposition from $Cu(acac)_2$ exhibits the spherical particle morphology expected of copper seeds on the CNT roving. Fig. S4d shows higher atomic number regions coincident with the spherical particles under BSE imaging which, combined with the emergence of a copper peak in EDS shown in Fig. S4g confirms that these particles are deposited copper seeds. The high contact angles of these spherical copper particles indicate limited adhesion and interaction with the CNT roving, represented in Fig. 1b, in line with the previously reported results [23]. In contrast, the prototypical deposition from platinum (II) acetylacetonate $Pt(acac)_2$, shown in Fig. 1c, led to tightly bound platinum clusters on the CNT roving substrate. As with the copper seeds, BSE imaging in Fig. S4f and EDS data in Fig. S4g confirm that the smaller clusters are platinum. Compared to the copper particles with average diameters of ~40 nm, the platinum nodules within each cluster formed by the $Pt(acac)_2$ deposition had nearly an order of magnitude smaller diameter of ~5 nm, represented in Fig. 1d. The lack of Ostwald ripening and coalescence in the platinum seeds is likely a result of a more energetically favorable interaction with the CNT roving surface as well as the higher melting point of platinum (1,768°C) compared to copper (1,085°C). The smaller, more closely bound clusters of platinum should act as a much more effective interconnection and seed metal that the large, discrete copper particles. Therefore, platinum appears to be a promising alternative to compare to copper in the study of the impact of deposited seed mass and morphology.

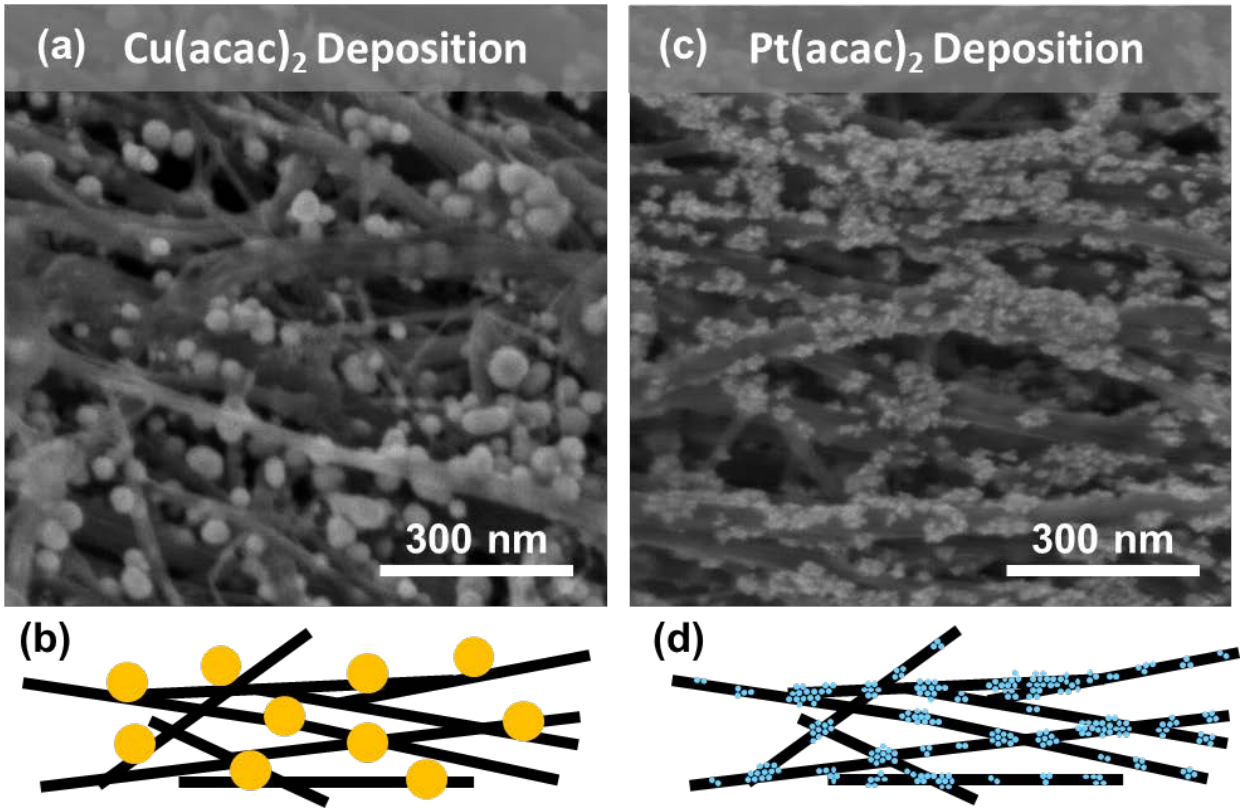

Fig. 1. (a) 1 hour DFH-CVD with 350 mA/roving, 25 mg $Cu(acac)_2$ precursor, 166 Torr. (b) Illustration of a loosely bound seeding type deposition, as from the $Cu(acac)_2$ precursor. (c) 1 hour DFH-CVD with 350 mA/roving, 25 mg $Pt(acac)_2$ precursor, 166 Torr. (d) Illustration of a more tightly bound seeding type deposition, as from the $Pt(acac)_2$ precursor.

The impact of precursor temperature on deposited mass was investigated by systematically varying the mantle temperature from 130°C to 210°C for a deposition of 50 mg $Cu(acac)_2$ in a one hour CFH-CVD at 166 Torr with 350 mA/roving current. The percent deposited metal mass is determined by dividing the mass added through the deposition by the mass of the seeded CNT conductor after the deposition. For example, a seeded CNT conductor that doubles in mass during the deposition would be calculated to be 50 % w/w metal. Fig. 2a demonstrates an increase in

deposited mass with increasing precursor temperature. At 130°C, composites of approximately 20 % w/w Cu are produced, with a coating of Cu seeds visible across the surface of the roving (Fig. 2b). A temperature of 130°C is the lowest value that can be reliably obtained in this CVD setup due to radiative or convective heating of the reaction vessel by the electrically biased CNTs. Representative images from depositions at 155°C (Fig. 2c), 175°C (Fig. 2d), and 210°C (Fig. 2e) show increasingly higher densities of seeds across the surface of the hybrid conductor, eventually completely obscuring sight of the underlying CNT roving. Likewise, the depositions at 155°C, 175°C, and 210°C led to progressively heavier mass loadings of 45 % w/w, 60 % w/w, and 65 % w/w Cu, respectively. Thus, the increase in precursor temperature increases the rate of sublimation and partial pressure of the precursor within the flask, allowing for higher deposited masses within the given deposition time. The deposition density begins to plateau due to exhaustion of the precursor around 200°C. Above 210°C, dark patches were observed on the bottom half of the flask from decomposition of the $Cu(acac)_2$ precursor, as expected above that temperature [36]. Heavier surface depositions lead to a general decrease in the R/L of the samples, as shown in Fig. S5, due to the eventual coalescence of the surface particles as a film. Thus, control over precursor temperature is one mechanism that allows for control over deposited mass due to modification of precursor's vapor pressure within the reaction chamber.

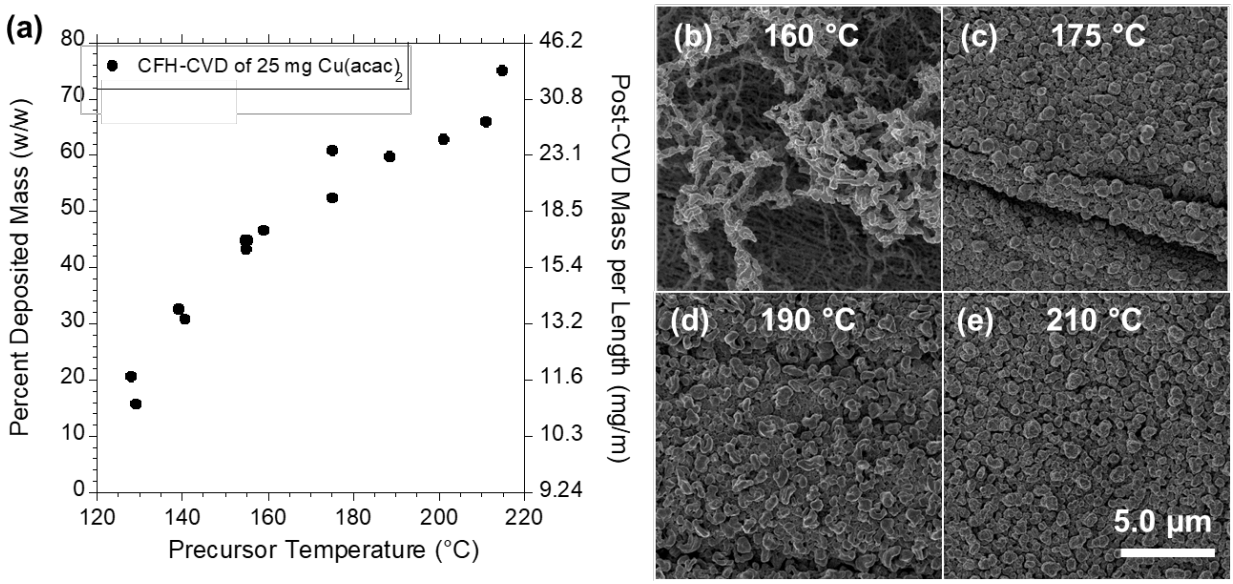

Fig. 2. (a) Impact of precursor temperature on deposited mass from $Cu(acac)_2$ precursor. Secondary electron images of depositions with mantle temperatures of (b) 160°C, (c) 175°C (d) 190°C (e) 210°C. Samples prepared via a 1 hour CFH-CVD with 350 mA/roving, with 25 mg $Cu(acac)_2$ precursor.

Complementary to precursor temperature, the effect of the CVD system pressure onto deposited mass and nanoscale morphology is evaluated in depositions from the $Cu(acac)_2$ precursor. CFH-CVD of 25 mg $Cu(acac)_2$ at 200°C with decreasing system pressure from 166 Torr to 0.175 Torr results in progressively lower density of surface particles with similar mass loading, as shown in Fig. S6. In contrast to the decrease in R/L (Fig. S5) measured from the heavier surface depositions produced at 166 Torr, the average resistance/length measured (390 ± 11 Ω/m) from the lighter surface depositions of the samples produced at 1 Torr, 0.300 Torr, and 0.170 Torr is slightly higher than that dried CNT roving. The results are consistent with lower system pressure increasing the mean free path of the vapor phase precursor and its mass fraction within the gaseous phase, leading

to improved infiltration of the vapor into the CNT network. Therefore, where modification of the precursor temperature allows for similar distributions of the nanometal particles at different mass loadings, adjustment of the chamber pressure allows for different nanometal distributions with similar mass loading by altering the mean free path of the vapor phase precursor through the heated CNT roving.

An additional factor that can influence the deposition mass and morphology when performing Joule heating driven CVD is the time interval over which the current for deposition is applied to the CNT roving. Here, a comparison is made between a continuously applied current in the CFH-CVD process and the delayed application of current in the DFH-CVD process. The comparison of the CFH-CVD and DFH-CVD procedures was carried out with one hour depositions of 25 mg of either $Cu(acac)_2$ or $Pt(acac)_2$ precursor at 200°C, applied current of 350 mA/roving, and a pressure of 0.300 Torr. SEM images show that the $Cu(acac)_2$ precursor deposits nanoscale spherules under both DFH-CVD (Fig. 3a) and CFH-CVD conditions (Fig. 3b). However, the DFH-CVD conditions with $Cu(acac)_2$ lead to substantially lighter depositions of 3.62 ± 0.63 % w/w compared to the CFH-CVD deposited masses of 63.7 ± 1.9 % w/w. In comparison, while the $Pt(acac)_2$ precursor leads to tightly bound deposited particles under the DFH-CVD condition (shown in Fig. 3), the SEM images indicate that under the CFH-CVD condition the platinum particles merged during deposition into more uniform coatings along the CNT bundles (shown in Fig. 3d). Similar to the copper precursor, DFH-CVD of 25 mg $Pt(acac)_2$ leads to much lighter deposited masses of 19.1 ± 6.0 % w/w than the 69.5 ± 5.0 % w/w deposited via CFH-CVD. The lower masses obtained by DFH-CVD are attributed to the fact that only the precursor that initially condenses onto the surface of the CNT roving is available for decomposition when the current is applied at the end of the one hour period. Thus, the CFH-CVD makes more efficient utilization of the available

precursor mass than the DFH-CVD approach, while the latter proves useful for producing lightweight depositions.

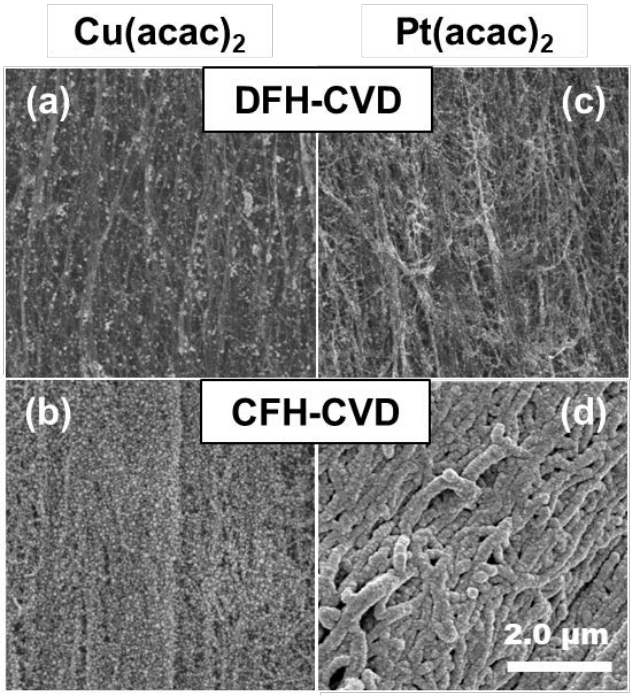

Fig. 3. Deposited particle morphology from DFH-CVD of the (a) $Cu(acac)_2$ and (c) $Pt(acac)_2$ precursors compared to particle morphology from CFH-CVD of the (b) $Cu(acac)_2$ and (d) $Pt(acac)_2$ precursors. Samples were prepared via 1 hour CVD with 350 mA/roving, 25 mg precursor at 200°C, and 0.300 Torr.

Previous work [23] demonstrated that the temperature of the CNT roving, controlled by the applied current, can impact the mass, morphology, and distribution of deposited particles. A similar study is carried out in the present work through modification of the applied current. A control experiment is carried out outside of the reaction flask in air where currents of 150–

350 mA/roving (0.45–1.05 A total) are applied to three CNT roving in parallel, and the resultant temperatures are measured. While temperatures within the flask under vacuum are undoubtedly higher, this provides a baseline understanding of the temperatures reached by the CNT roving. From the results shown in Fig. S3, average temperatures of 94.1°C at 150 mA/roving, 129°C at 200 mA/roving, 168°C at 250 mA/roving, 197°C at 300 mA/roving, and 224°C at 350 mA/roving are observed. While the average temperature is relatively low, the maximum measured temperature at 200 mA/roving of 186°C approaches the decomposition onset temperature range of 225–250°C for the $Cu(acac)_2$ [36] and $Pt(acac)_2$ [35] precursors. Therefore, 200 mA/roving is chosen as the lower limit for the applied deposition current study. The upper limit of 350 mA/roving represents the highest current the roving can consistently handle in this setup without undergoing failure.

In the study of applied deposition currents, conditions were constant with one hour CFH depositions using 10 mg $Cu(acac)_2$ or $Pt(acac)_2$ precursor at 200°C and 0.300 Torr with three CNT roving in parallel. Increases in mass, indicating depositions from each of the precursors, are observed at all currents from 200 mA to 350 mA, as shown in Fig. 4a. This indicates temperatures in excess of the 225–250°C required for decomposition of the metal-organic precursors [35,36]. Across the entire 200–350 mA/roving current range, the deposited masses from copper were relatively invariant between 20–30 % w/w. In comparison, deposited mass from $Pt(acac)_2$ was observed to increase with increasing current from an average of 16.1 % w/w at 200 mA/roving to 58.1 % w/w at 350 mA/roving. The SEM results for the $Cu(acac)_2$ depositions given in Fig. 4b-e show spherical copper particles at all applied roving currents, indicative of the limited interaction between the deposited copper and the CNT roving. The SEM results for the $Pt(acac)_2$ depositions demonstrate the tightly bound platinum clusters between 200–250 mA/roving (Fig. 4f-g), transitioning to more uniform coatings from 300–350 mA/roving (Fig. 4h-i). Previous work

demonstrated that at lower currents, only certain localized hot-spots reach temperatures sufficient for deposition [23]. The invariance of the copper mass and particle morphology could be attributed to its limited physical and electrical interaction with the CNT substrate. Since the copper forms disconnected spheres rather than coatings on the CNT roving network, it is expected that such hot-spots remain hot, leading to continual deposition from the $Cu(acac)_2$ precursor. In fact, the resistance measured from the two electrical leads during the depositions was only seen to decrease by an average of 2.5 % for the $Cu(acac)_2$ CFH-CVD. Consequently, at lower currents there may be a higher proportion of the total copper deposited at the high temperature hot-spot locations (i.e. a site-specific deposition [23]), but the total mass of deposited copper does not change. In contrast, the more tightly adhered platinum forms coatings and interconnections with less metal volume than the copper. The $Pt(acac)_2$ CFH-CVD shows an average decrease of 10.4 % in the resistance measured from the two electrical leads during the depositions, 4X the magnitude of the decrease from the $Cu(acac)_2$ CFH-CVD. Thus, it is possible that these interconnections can lower the local resistance at the hot-spots and cools those locations below the decomposition temperature, thereby preventing further deposition from the $Pt(acac)_2$ precursor. Therefore, until the entire CNT roving exceeds the decomposition temperature of the $Pt(acac)_2$ precursor the deposited mass of platinum would be expected to increase proportionally to the applied current, as more metal is required to electrically interconnect the increasing proportion of high temperature sites on the CNT roving. Overall, it can be concluded that while it is possible for copper to be able to deposit site-specifically at higher temperature locations, only the platinum appears to be able to electrically interconnect the CNT network to cool such high temperature locations.

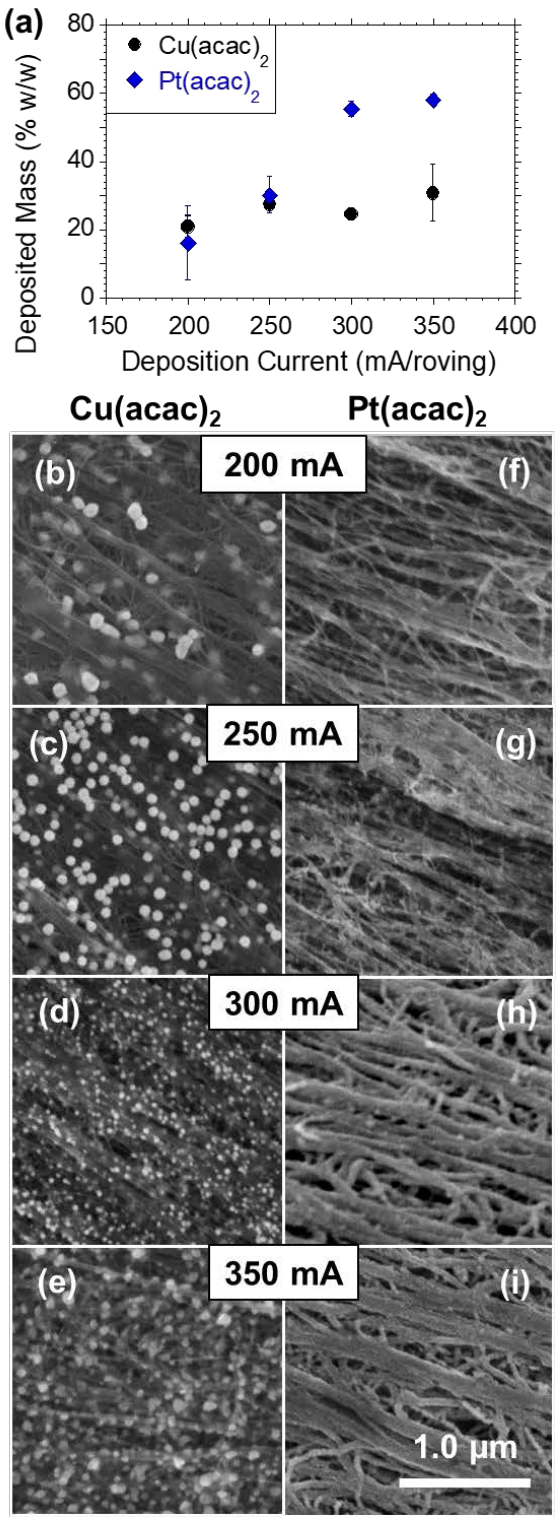
(a)
Deposited Mass (% w/w)
Deposition Current (mA/roving)
Cu(acac)2
Pt(acac)2
0
20
40
60
80
150
200
250
300
350
400
Cu(acac)2
Pt(acac)2
(b)
200 mA
(f)
(c)
250 mA
(g)
(d)
300 mA
(h)
(e)
350 mA
(i)
1.0 µm

Fig. 4. (a) Impact of current per roving on deposited particle mass. Secondary electron micrographs from (b-e) $Cu(acac)_2$ and (f-i) $Pt(acac)_2$ precursors. Samples were prepared via a 1 hour CFH-CVD, 10 mg precursor at 200°C, and 0.300 Torr.

The influence of precursor mass to drive reaction dynamics was also evaluated. As the entire mass of precursor is sublimated within the deposition time, increases in precursor mass in the flask leads to increased availability of vapor for deposition. The results of one hour depositions of precursor masses of 5, 10, 25, and 50 mg at 200°C and 0.300 Torr onto three CNT roving in parallel electrically biased to 350 mA/roving are presented in Fig. 5a. As expected, deposited masses from both $Cu(acac)_2$ and $Pt(acac)_2$ are observed to increase with increasing precursor mass. The depositions from $Pt(acac)_2$ are slightly heavier at each precursor mass due to the higher mass percentage of platinum in $Pt(acac)_2$ (49.6 % w/w) compared to copper in $Cu(acac)_2$ (24.3 % w/w). However, the volume of metal available in each gram of precursor is similar, with 2.3×10^{-2} cm^3/g of platinum in $Pt(acac)_2$ and 2.7×10^{-2} cm^3/g of copper in $Cu(acac)_2$. Thus, the deposited volume of copper is actually greater than that of the platinum in the 25 mg and 50 mg depositions (as plotted in Fig. S7). In the $Cu(acac)_2$ depositions, particle morphology is maintained regardless of the deposited mass (Fig. 5b-e), with heavier deposited masses exhibiting increasingly dense clusters of spherical nanoparticles. In the $Pt(acac)_2$ deposition, a transition is noted between the 5 mg precursor deposition (Fig. 5f) and the 10 mg precursor deposition (Fig. 5g), where tightly bound nanoparticles give way to uniform coatings over the surface of the nanotubes. The platinum coatings become more dense and rough as the starting precursor mass increases to 25 mg (Fig. 5h) and 50 mg (Fig. 5i), as platinum fills in the interstitial space between CNT bundles. Overall, copper exhibits similar spherical morphology at all masses measured, while platinum exhibits small

tightly bound particles at lighter mass loadings giving way to cohesive films at heavier mass loadings.

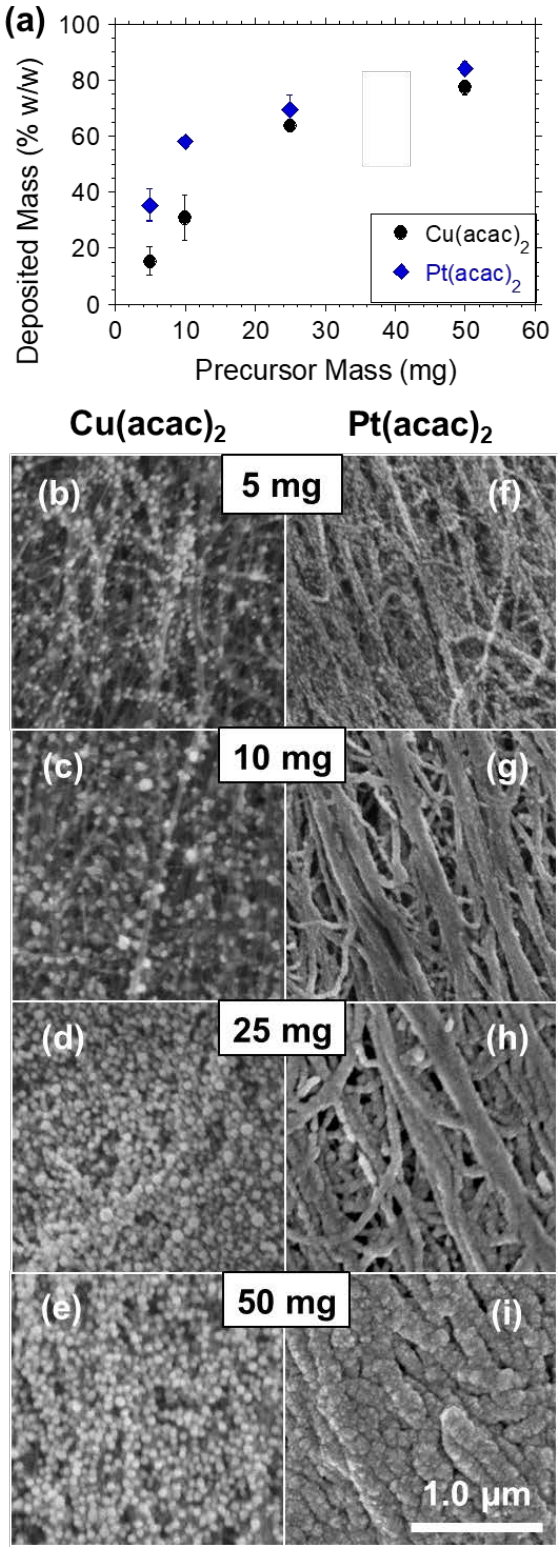
(a)
Deposited Mass (% w/w)
Precursor Mass (mg)
Cu(acac)2
Pt(acac)2
Cu(acac)2
Pt(acac)2
(b)
5 mg
(f)
(c)
10 mg
(g)
(d)
25 mg
(h)
(e)
50 mg
(i)
1.0 μm

Fig. 5. (a) Impact of precursor mass on deposited mass. Secondary electron micrographs from (b-e) $Cu(acac)_2$ and (f-i) $Pt(acac)_2$ precursors. Samples prepared via a 1 hour CFH-CVD with 350 mA/roving, precursor at 200°C, 0.300 Torr.

The bulk electrical characterization at room temperature for all the samples described to this point is presented in Fig. 6. The R/L of the $Cu(acac)_2$ seeded samples are generally higher than the dried CNT roving, as shown in Fig. 6a. In contrast, the $Pt(acac)_2$ seeded samples exhibit lower R/L than the CNT roving over nearly all mass loadings. The greatest decreases in R/L were noted between 20–50 % w/w deposited platinum mass, with some samples exhibiting nearly 40% reduction from the dried CNT roving. The R/L data in Fig. 6a demonstrates that the copper depositions are not enhancing electrical transport, but rather acting as electronic scattering sites. In comparison, the lower R/L of the platinum samples indicates improvement to the electronic transport, and the platinum may be acting as electrical interconnections between the CNT bundles.[40] Measurement of the mass per length (M/L) allows for calculation of the specific conductivity, which gives an indication of the improvements to the conductance on a mass specific basis, i.e. whether improvements in R/L are greater than the added mass. The specific conductivity is calculated by multiplying the reciprocal of the R/L by the reciprocal of the M/L, which is equivalent to normalizing the electrical conductivity to the conductor's density [6,41,42]. In this study the specific conductivity can provide a quantification of the degree of utilization of deposited metal mass in the electrical conductor [23]. As can be seen from the resulting data (Fig. 6b), the greatest improvements to specific conductivity are observed in the $Pt(acac)_2$ seeded samples with < 50 % w/w platinum mass, with top performing samples around 30 % w/w platinum mass.

Consistent with the R/L data, the $Pt(acac)_2$ seeded samples outperform the Cu seeded samples across all mass loadings in specific conductivity. This is particularly notable because copper has a specific conductivity over 10× greater than platinum. While improvements to electrical conductance through site-specific CVD of metals have been noted at the nanoscale [40], the results presented here demonstrate the initial applicability using platinum for this technique to bulk CNT electrical conductors.

Along with the encouraging improvements to R/L and specific conductivity of the $Pt(acac)_2$ seeded samples, the case for interconnection would be enhanced through the measurement of a low TCR. Fig. 6c plots the change in resistance relative to 300 K of the dried CNT roving, $Pt(acac)_2$ seeded samples with deposited masses from 31 to 86 w/w% platinum (from the series presented in Fig. 5a), and the literature values for platinum [43] with increasing temperature. For linear trends, such as that of the $Pt(acac)_2$ seeded CNTs, the TCR relative to 300 K (TCR_{300K}) can be calculated from the slope of the resistance relative to its value at 300 K over the temperature range [44]. While the dried roving does not exhibit a strictly linear trend in its relative resistance, an approximation of the TCR_{300K} using the linear method was calculated to be 2.18×10^{-4} K^{-1}. The measured series of samples with 31 to 86 w/w% platinum all exhibit similar increases in relative resistance from 300 K to 600 K. For the $Pt(acac)_2$ seeded samples, the TCR_{300K} ranges from 0.57×10^{-3} K^{-1} to $0.71 \pm 0.06 \times 10^{-3}$ K^{-1} over this range of masses. These TCR_{300K} values are on the same order of magnitude as the linear approximation for the as-received CNT roving, and approximately an order of magnitude lower than the literature value for platinum (3.47×10^{-3} K^{-1}) [43]. Overall, the relative invariance to platinum metal loading for the temperature dependent electrical properties over this wide range of masses suggests electrical interconnection between

the platinum and carbon nanotube fractions, especially when considered in combination with the improvements to specific conductivity.

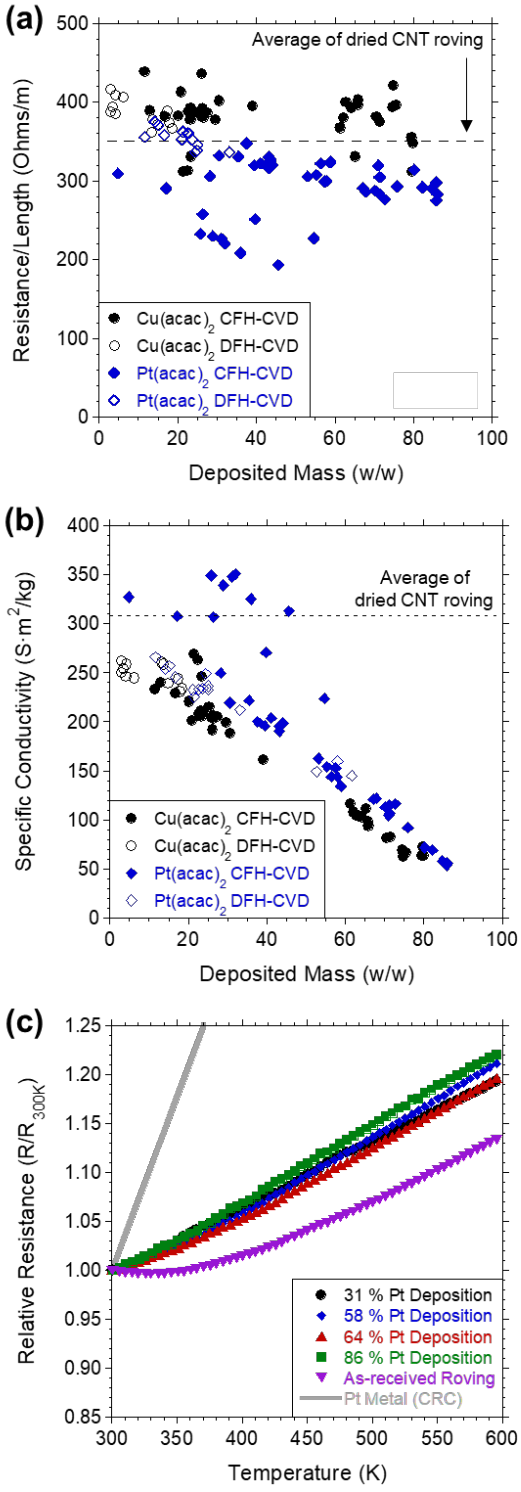

Fig. 6. Summary of (a) resistance per length and (b) specific conductivity of varying mass depositions from CFH-CVD of $Pt(acac)_2$ and $Cu(acac)_2$ onto CNT Roving. (c) Relative resistance of CFH-CVD seeded samples from various precursors masses compared to platinum and as-received roving. 1 hour CFH-CVD with 350 mA/roving, precursor at 200°C, 0.300 Torr.

To demonstrate the versatility of the Joule heating driven CVD technique and provide a thorough comparison to copper and platinum, other periodic group 10 (Ni, Pd) and platinum group (Pd, Ru, Rh, Ir) metals are deposited. For each metal, a lighter (from 5 mg precursor) and heavier (from 25 mg precursor) CFH-CVD are carried out with three roving in parallel electrically biased to 350 mA/roving with a 200°C mantle temperature at 0.300 Torr pressure. The EDS results in Fig. S8 demonstrate the advent of the corresponding metal peaks from each deposition, indicating that the depositions were successful. Secondary electon images of each deposition are presented in Fig. 7. An additional magnification and BSE images for each of these precursors are available in Fig. S9. The 5 mg $Ni(acac)_2$ deposition produces irregular nodules along the surface of the roving at 30.2 ± 8.9 % w/w, shown in Fig. 7a. The deposition transitions to an uneven nodular coating over the entire CNT roving surface at 68.0 ± 8.5 % w/w from 25 mg $Ni(acac)_2$, shown in Fig. 7b. The irregularity of these large nodules and their inconsistent contrast in BSE imaging could indicate carbon contamination from the precursor in the deposited nickel, a phenomenon which has been observed in water-free depositions from $Ni(acac)_2$ [45]. Fig. 7c shows that the 5 mg $Pd(acac)_2$ deposition produces a very rough, although consistent coating over the CNT roving surface at 27.3 ± 4.1 %. With the heavier 25 mg $Pd(acac)_2$ deposition shown in Fig. 7d, the rough coating begins to fill in the gaps between the CNT bundles with an increase in deposited mass to 61.3 ± 0.9 %. From CFH-CVD of 5 mg $Ru(acac)_3$, clusters and small nodules are visible in Fig. 7e at 10.5 ± 2.9 % w/w. The 25 mg $Ru(acac)_3$ deposition produces a mass loading of

32.9 ± 2.5 % w/w, with the particles transitioning to a tight, irregular coating shown in Fig. 7f. The $Rh(acac)_3$ deposited small nanoparticles from 5 mg of precursor, as shown in Fig. 7g, transitioning to uniform coatings from 25 mg of precursor, as shown in Fig. 7h. The deposited masses from the 5 mg and 25 mg $Rh(acac)_3$ depositions were 13.3 ± 3.0 % w/w and 57.0 ± 5.1 % w/w, respectively. CFH-CVD of 5 mg $Ir(acac)_3$, shown in Fig. 7i, produced a mixture of nodules and an irregular coating at 17.6 ± 4.3 % w/w. The 25 mg $Ir(acac)_3$ deposition produced a uniform coating of variable thickness with a deposited mass of 63.8 ± 3.2 % w/w, as can be seen in Fig. 7j. The electrical performance of these conductors is summarized in Fig. S10. Nickel produced similar increases in R/L to copper, with larger masses leading to higher R/L. Palladium, ruthenium, rhodium, and iridium all exhibited lower R/L at higher mass loadings than at low mass loadings. This may indicate a critical particle density necessary for improvements in conductivity to become apparent. Decreases in R/L were observed from both mass loadings of iridium. This suggests that, like platinum, the smoother coatings and smaller particles indicate better electrical interaction with the underlying CNTs, which leads to improved interconnection of the CNT substrate. Overall however, the decreases in R/L exhibited by platinum, particularly at low mass loadings, indicate that platinum is still the preferred candidate for nanometal interconnection and seeding.

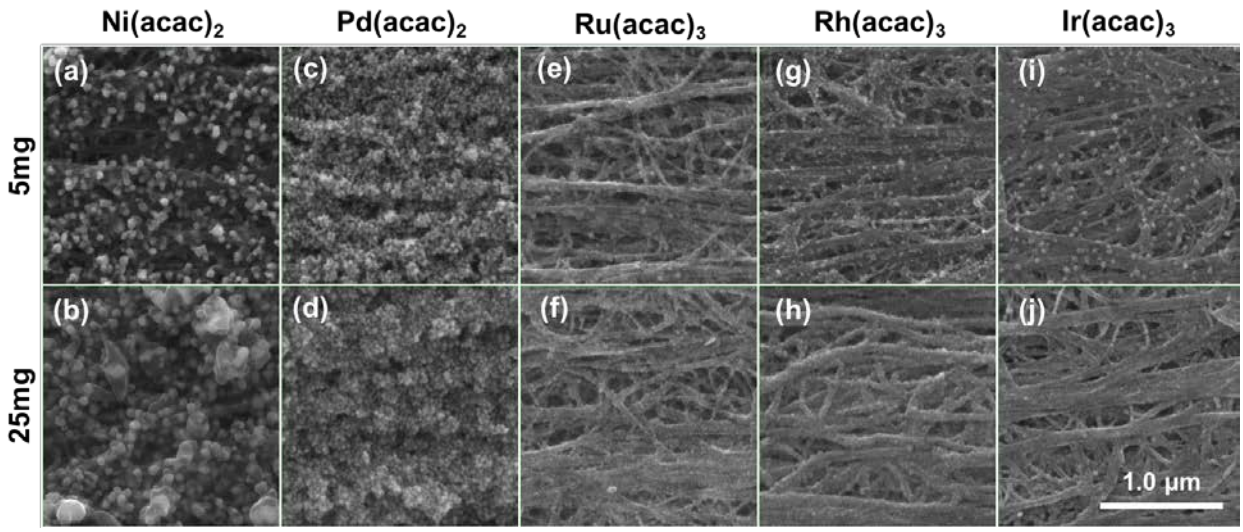

Fig. 7: Secondary electron micrographs from one hour CFH-CVD at 200°C with three roving in parallel at 350 mA/roving of (a) 5 mg $Ni(acac)_2$, (b) 25 mg $Ni(acac)_2$, (c) 5 mg $Pd(acac)_2$, (d) 25 mg $Pd(acac)_2$, (e) 5 mg $Ru(acac)_3$, (f) 25 mg $Ru(acac)_3$, (g) 5 mg $Rh(acac)_3$, (h) 25 mg $Rh(acac)_3$, (i) 5 mg $Ir(acac)_3$, and (i) 25 mg $Ir(acac)_3$.

3.2. Production of $Pt(acac)_2$ Seeded Cu-CNT Conductors via Electroplating

The collective results from SEM and electrical measurements lead to the conclusion that platinum is an effective interconnection metal over the range of 20–50 % w/w metal. Therefore, CNT roving with ~30 % w/w platinum seeds deposited via DFH-CVD and CFH-CVD were subsequently processed into hybrid electrical conductors via electroplating, densification, and annealing similar to our previous approach [23]. Here, three constant current electroplating rates of 9.4, 11, and 15 A/g were chosen to study the impact of plating rate on the infiltration of copper in samples produced through DFH-CVD. The plating time was adjusted to achieve a similar average total metal mass of 94.5 ± 0.2 % w/w. The electroplated samples were then finished by

densification in a rolling mill and annealing at 300°C for 3 hours in 5 % H_2/95 % Ar gas. As shown in Fig. 8a, the slowest plating rate (9.4 A/g) exhibited the smallest increase in resistance with temperature, equating to a TCR_{300K} of 3.12×10^{-3} K^{-1}. The middle plating rate (11 A/g) exhibited an increase in resistance somewhere between the faster and slower rate, with a TCR_{300K} of 3.33×10^{-3} K^{-1}. Finally, the fastest plating rate (15 A/g) exhibited the greatest increase in resistance with temperature, equating to a TCR_{300K} of 3.50×10^{-3} K^{-1}. Previous literature regarding the production of Cu-CNT conductors indicate that low TCR in a hybrid electrical conductor is a result of good intermixing of the CNT and metal portions of the conductor [9,10,17,46]. In this study, faster plating rates are also correlated with higher specific conductivities. The specific conductivities are 4126 $S \cdot m^2/kg$ for the 9.4 A/g plating rate, 4776 $S \cdot m^2/kg$ for the 11 A/g plating rate, and 5772 $S \cdot m^2/kg$ for the 15 A/g plating rate. These combinations of specific conductivity and TCR agree well with the theory of infiltration: heavier copper surface coatings produced through faster plating rates are more conductive but less electrically integrated with the underlying seeded CNTs, thus producing higher temperature coefficients. The sample seeded via CFH-CVD of $Pt(acac)_2$ was electroplated at a rate of 7.6 A/g. This sample exhibited a similar TCR_{300K} (3.33×10^{-3} K^{-1}) and specific conductivity (4519 $S \cdot m^2/kg$) to the DFH-CVD samples, demonstrating that both deposition techniques achieve similar results. Overall, a balance exists at this mass loading between infiltration of the hybrid with copper and maintaining sufficient copper cohesion to achieve high specific conductivity.

A useful approach described previously [23] for probing the interaction between the metal and CNT fraction of a hybrid electrical conductor is to compare the specific conductivity and temperature coefficient of resistance for the conductor to the values expected from a non-interacting system of parallel copper and CNT electrical conductors. Such a system can be

modeled across all mass percentages of copper and CNTs, producing a curve as shown in Fig. 8b spanning from 100 % CNTs to 100 % copper. Conductors with a combination of a lower TCR and higher specific conductivity than expected from this parallel-conductors model indicate a favorable interaction between the metal and CNT portions of the conductor. Such conductors are positioned above the curve on Fig. 8b. As can be seen from the resulting data, each of the $Pt(acac)_2$ seeded, copper plated CNT conductors reside above the rule of mixtures curve indicating favorable interaction between the metals and CNTs. Additionally, the hybrid conductor produced at the 15 A/g electroplating rate shows an improvement over previously published results [23], with slight improvements to both specific conductivity and TCR. These results demonstrate the utility of platinum as an interconnection metal, as well as serving as an enhanced seed metal for copper electroplating in a hybrid design.

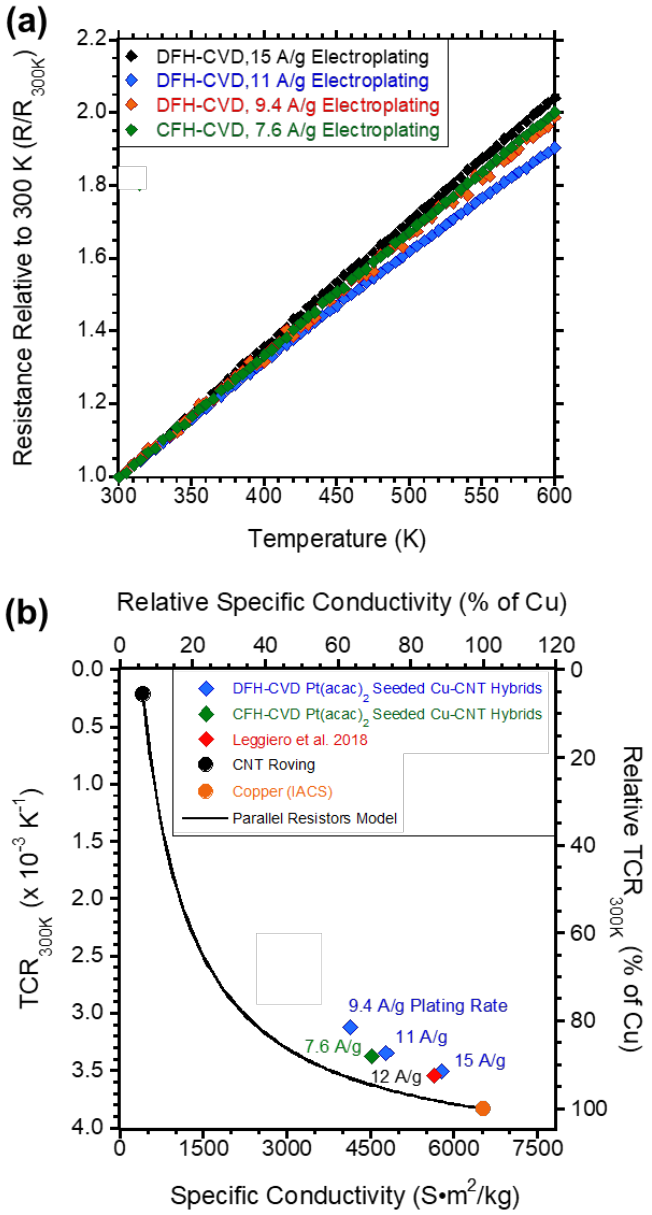

Fig. 8. (a) Relative resistance of samples electroplated to 94.5% w/w total metal mass with various plating rates from samples with ~30% w/w platinum seed mass after DFH-CVD or CFH-CVD. (b) TCR and specific conductivity of samples plated with various plating rates compared to the parallel resistors model and previously published data [23]. Note the inverted y-axis (TCR_{300K}) on the plot.

The bulk electrical conductivity represents the electrical transport in a conductor adjusted for the cross-sectional area and can be used to compare with other reported hybrid conductors. SEM cross-sections were acquired for the platinum seeded Cu-CNT hybrids to determine the electrical conductivity and investigate the infiltration of the metal into the CNT roving. A representative SEM cross-section is provided in Fig. S11, with false color imaging used to indicate the region of interest. From the measured cross-sectional areas, conductivities for the DFH-CVD samples of 22.1 MS/m for the 9.4 A/g plating rate, 29.8 MS/m for the 11 A/g plating rate, and 29.3 MS/m for the 15 A/g plating rate are calculated. For the CFH-CVD sample, a conductivity of 26.9 MS/m for the 7.6 A/g plating rate is calculated. These values are among the highest reported at or below this mass loading of copper, as seen in Fig. 9a. These values are also on the same order of magnitude as those for traditional metals like copper (58 MS/m) and aluminum (38 MS/m). EDS of a cross-section (Fig. 9b) of the top-performing 11 A/g sample reveals the presence of platinum seeds (Fig. 9c) through the interior volume of the final conductor. While the signal from the electrodeposited copper (Fig. 9d) is much more prominent on the exterior of the hybrid conductor's surface, the microstructure of the interfacial area indicates a degree of integration due to the change in grain structure [47]. The carbon shows a complementary trend (Fig. 9e), indicating that the exterior of the electrical conductor is mostly copper. However, the iron signal (Fig. 9f), which arises form leftover catalyst enveloped within the CNT bundles, again indicates integration between the CNTs and copper. Finally, the nonspecific and dampened oxygen signal (Fig. 9g) indicates the presence of metals rather than oxides within the annealed conductor. The spectrum from the analyzed area is presented in Fig. S12 along with larger versions of the SEMs for additional reference. Overall, these results demonstrate the first instance of the use of CVD to produce a platinum-interconnected Cu-CNT conductor with electrical conductivity comparable to that of traditional metals.

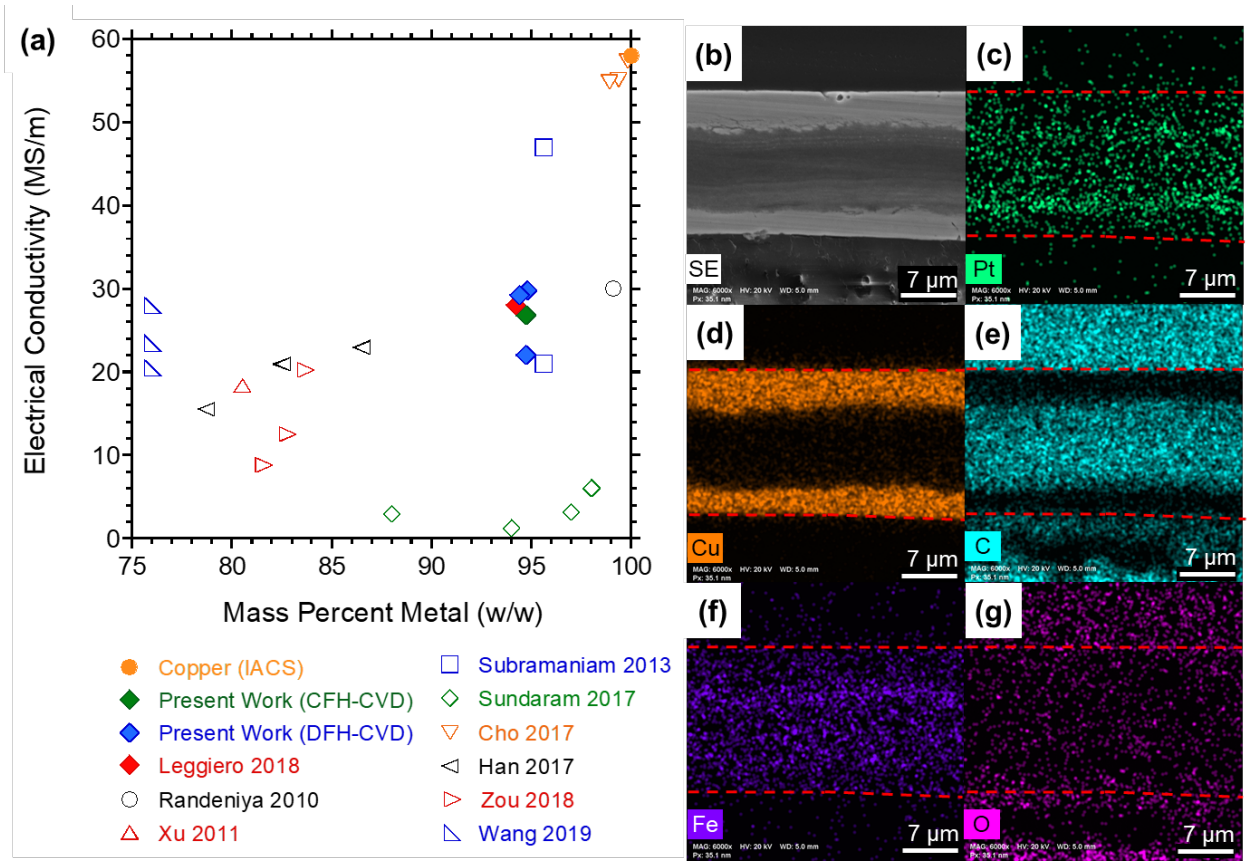

Fig. 9. (a) Conductivity of top performing samples compared to previous work [23] and the state of the field: Randeniya (2010) [2], Xu (2011) [12], Subramaniam (2013) [9], Sundaram (2017) [10], Cho (2017) [17], Han (2017) [18], Zou (2018) [13], and Wang (2019) [26]. (b) Secondary electron image of an epoxy set and microtomed cross-section from the $Pt(acac)_2$ seeded Cu-CNT conductor with the 11 A/g plating rate. EDS maps of the (c) Pt Lα signal (d) Cu Kα signal, (e) C Kα signal, (f) Fe Kα signal, and (g) O Kα signal each with the edges of the cross section outlined in red.

4. Conclusions

In this work, we have demonstrated the versatility of a site-selective Joule heating driven CVD technique towards the production of nanometal interconnected CNT hybrid conductors. Depositions from $Cu(acac)_2$, $Pt(acac)_2$, $Ni(acac)_2$, $Pd(acac)_2$, $Ru(acac)_3$, $Rh(acac)_3$, and $Ir(acac)_3$ have been carried out, and the impact of various processing parameters have been investigated. Deposited mass was controlled by modification of precursor temperature, with temperatures up to 200°C allowing for the complete sublimation of the acetylacetonate precursor and the highest deposited masses. Decreasing the system pressure from 166 Torr to 0.175 Torr produced similar mass loadings, but a lower density of surface particles. Thus, lower pressures seem to lead to a higher degree of infiltration of the nanometal vapor into the CNT roving. Further refinement to deposited masses can be made by modifying the interval of the applied heating current to the CNT roving, with masses as low as 5 % w/w obtained through DFH-CVD and masses as high as 85 % w/w obtained through CFH-CVD. Modification of the of applied current used to Joule-heat the CNT roving led to changes in the deposited particle morphology, with transition from site-specific $Pt(acac)_2$ depositions noted at 200–250 mA giving way to more uniform coatings from 300–350 mA. Average deposited seed mass and volume were also controlled by varying the amount of precursor in the reaction chamber, leading to sparse deposition at low precursors masses and heavier coverage at higher precursor masses. Generally, the platinum group elements (platinum, palladium, ruthenium, rhodium, and iridium) led to smaller particle sizes, more uniform coatings, and better post-deposition R/L than copper or nickel. The broad applications of the Joule heating driven CVD technique may have further uses towards catalysis, sensor, and shielding applications. Platinum seeds in particular displayed improved adhesion and interaction with the CNT roving substrate through its nanoscale particles and smooth coatings. Over the full range of masses investigated, the R/L of the seeded conductors was lower with depositions from $Pt(acac)_2$

than from $Cu(acac)_2$. Deposition from $Pt(acac)_2$ with masses less than 50 % w/w led to the greatest improvements in specific conductivity of the seeded CNT conductors. Platinum depositions from 31–86 % w/w all exhibited TCR_{300K} much closer to that of the CNT roving than bulk platinum metal, indicating good interaction between the seed metal and CNTs. To the best of the authors' knowledge, this is the first demonstration of the use of platinum nanometal interconnection in a bulk CNT conductor. Electroplated, densified and annealed hybrid conductors produced from samples with ~30 % w/w platinum exhibited combinations of TCR and specific conductivity better than that expected from non-interacting parallel conductors, indicating integration of the metal and CNT portions of the hybrid. Finally, electrical conductivities of up to 29.8 MS/m at room temperature were obtained, approaching conventional metals like copper (58 MS/m) and aluminum (38 MS/m).

SUPPLEMENTARY MATERIAL:

Supplementary Figures (.pdf)

AUTHOR INFORMATION

Author Contributions

The manuscript was written through contributions of all authors. All authors have given approval to the final version of the manuscript.

ACKNOWLEDGEMENT

The authors would like to thank R. Rogers, M. Schauer, and E. Zeira for helpful discussions. The authors acknowledge funding from the Advanced Manufacturing Office of the Office of

Energy Efficiency and Renewable Energy of the U.S. Department of Energy under grant DE-EE0007863. The contents of this document should not be construed as asserting or implying U.S. Government authentication of information or endorsement of the authors' views.

ABBREVIATIONS

BSE, backscatter electron; CFH, continuous filament heating; CNT, carbon nanotube; $Cu(acac)_2$, copper (II) acetylacetonate; Cu-CNT, copper-carbon nanotube; $Cu(tBAOAC)_2$, bis(t-butylacetoacetato) copper (II); CVD, chemical vapor deposition; DFH, delayed filament heating; EDS, energy dispersive x-ray spectroscopy; $Ir(acac)_3$, iridium (III) acetylacetonate; IV sweep, current-potential sweep; M/L, mass per length; $Ni(acac)_2$, nickel (II) acetylacetonate; $Pd(acac)_2$, palladium (II) acetylacetonate; $Pt(acac)_2$, platinum (II) acetylacetonate; $Rh(acac)_3$, rhodium (III) acetylacetonate; $Ru(acac)_3$, ruthenium (III) acetylacetonate; R/L, resistance per length; SE, secondary electron; SEM, scanning electron microscopy; TCR, temperature coefficient of resistance

REFERENCES

[1] National Bureau of Standards, Copper wire tables, 3rd ed., Washington, D.C., 1914.

[2] L.K. Randeniya, A. Bendavid, P.J. Martin, C.D. Tran, Composite yarns of multiwalled carbon nanotubes with metallic electrical conductivity, Small. 6 (2010) 1806–1811. https://doi.org/10.1002/smll.201000493.

[3] J. Lee, I.Y. Stein, M.E. Devoe, D.J. Lewis, N. Lachman, S.S. Kessler, S.T. Buschhorn, B.L. Wardle, Impact of carbon nanotube length on electron transport in aligned carbon nanotube networks, Appl. Phys. Lett. 106 (2015) 053110. https://doi.org/10.1063/1.4907608.

[4] N. Behabtu, C.C. Young, D.E. Tsentalovich, O. Kleinerman, X. Wang, A.W.K. Ma, E.A. Bengio, R.F. Ter Waarbeek, J.J. De Jong, R.E. Hoogerwerf, S.B. Fairchild, J.B. Ferguson, B. Maruyama, J. Kono, Y. Talmon, Y. Cohen, M.J. Otto, M. Pasquali, Strong, light, multifunctional fibers of carbon nanotubes with ultrahigh conductivity, Science (80-.). 339 (2013) 182–186. https://doi.org/10.1126/science.1228061.

[5] P. Jarosz, C. Schauerman, J. Alvarenga, B. Moses, T. Mastrangelo, R. Raffaelle, R. Ridgley, B. Landi, Carbon nanotube wires and cables: Near-term applications and future perspectives, Nanoscale. 3 (2011) 4542–4553. https://doi.org/10.1039/c1nr10814j.

[6] A. Lekawa-Raus, J. Patmore, L. Kurzepa, J. Bulmer, K. Koziol, Electrical properties of carbon nanotube based fibers and their future use in electrical wiring, Adv. Funct. Mater. 24 (2014) 3661–3682. https://doi.org/10.1002/adfm.201303716.

[7] A. Lekawa-Raus, T. Gizewski, J. Patmore, L. Kurzepa, K.K. Koziol, Electrical transport in carbon nanotube fibres, Scr. Mater. 131 (2017) 112–118. https://doi.org/10.1016/j.scriptamat.2016.11.027.

[8] B.T. Moses, R.P. Raffaelle, P.R. Jarosz, C.D. Cress, C.M. Schauerman, J. Alvarenga, B.J. Landi, High conductivity carbon nanotube wires from radial densification and ionic doping, Appl. Phys. Lett. 97 (2010) 182106. https://doi.org/10.1063/1.3506703.

[9] C. Subramaniam, T. Yamada, K. Kobashi, A. Sekiguchi, D.N. Futaba, M. Yumura, K. Hata, One hundred fold increase in current carrying capacity in a carbon nanotube–copper composite, Nat. Commun. 4 (2013) 1–7. https://doi.org/10.1038/ncomms3202.

[10] R. Sundaram, T. Yamada, K. Hata, A. Sekiguchi, Electrical performance of lightweight

CNT-Cu composite wires impacted by surface and internal Cu spatial distribution, Sci. Rep. 7 (2017) 9267. https://doi.org/10.1038/s41598-017-09279-x.

[11] P. Hannula, M. Junnila, D. Janas, J. Aromaa, O. Fors, M. Lundstr, Carbon Nanotube Fiber Pretreatments for Electrodeposition of Copper, Adv. Mater. Sci. Eng. 2018 (2018). https://doi.org/10.1155/2018/3071913.

[12] G. Xu, J. Zhao, S. Li, X. Zhang, Z. Yong, Q. Li, Continuous electrodeposition for lightweight, highly conducting and strong carbon nanotube-copper composite fibers, Nanoscale. 3 (2011) 4215–4219. https://doi.org/10.1039/c1nr10571j.

[13] J. Zou, D. Liu, J. Zhao, L. Hou, T. Liu, X. Zhang, Y. Zhao, Y.T. Zhu, Q. Li, Ni Nanobuffer Layer Provides Light-Weight CNT/Cu Fibers with Superior Robustness, Conductivity, and Ampacity, ACS Appl. Mater. Interfaces. 10 (2018) 8197–8204. https://doi.org/10.1021/acsami.7b19012.

[14] A. Lekawa-Raus, P. Haladyj, K. Koziol, Carbon nanotube fiber-silver hybrid electrical conductors, Mater. Lett. 133 (2014) 186–189. https://doi.org/10.1016/j.matlet.2014.06.177.

[15] C. Laurent, C. Estournès, N. Ferreira, G. Chevallier, C. Josse, A. Weibel, D. Mesguich, F. Lecouturier, C. Arnaud, High strength-high conductivity carbon nanotube-copper wires with bimodal grain size distribution by spark plasma sintering and wire-drawing, Scr. Mater. 137 (2017) 78–82. https://doi.org/10.1016/j.scriptamat.2017.05.008.

[16] C. Arnaud, F. Lecouturier, D. Mesguich, N. Ferreira, G. Chevallier, C. Estournès, A. Weibel, C. Laurent, High strength – High conductivity double-walled carbon nanotube – Copper composite wires, Carbon N. Y. 96 (2015) 212–215.

https://doi.org/10.1016/j.carbon.2015.09.061.

[17] S. Cho, K. Kikuchi, E. Lee, M. Choi, I. Jo, S.-B. Lee, S.-K. Lee, A. Kawasaki, Chromium carbide/Carbon Nanotube Hybrid Structure Assisted Copper Composites with Low Temperature Coefficient of Resistance, Sci. Rep. 7 (2017) 14943. https://doi.org/10.1038/s41598-017-14915-7.

[18] B. Han, E. Guo, X. Xue, Z. Zhao, L. Luo, H. Qu, T. Niu, Y. Xu, H. Hou, Fabrication and densification of high performance carbon nanotube/copper composite fibers, Carbon N. Y. 123 (2017) 593–604. https://doi.org/10.1016/j.carbon.2017.08.004.

[19] B. Han, E. Guo, X. Xue, Z. Zhao, T. Li, Y. Xu, L. Luo, H. Hou, Fabricating and strengthening the carbon nanotube/copper composite fibers with high strength and high electrical conductivity, Appl. Surf. Sci. 441 (2018) 984–992. https://doi.org/10.1016/j.apsusc.2018.02.078.

[20] B. Han, E. Guo, X. Xue, Z. Zhao, T. Li, Y. Xu, L. Luo, H. Hou, Enhancement of the twisted carbon nanotube fibers properties by drawing processing and acid treatment, Mater. Des. 143 (2018) 238–247. https://doi.org/10.1016/j.matdes.2018.02.004.

[21] T.Q. Tran, J.K.Y. Lee, A. Chinnappan, W.A.D.M. Jayathilaka, D. Ji, V.V. Kumar, S. Ramakrishna, Strong, lightweight, and highly conductive CNT/Au/Cu wires from sputtering and electroplating methods, J. Mater. Sci. Technol. 40 (2020) 99–106. https://doi.org/10.1016/j.jmst.2019.08.033.

[22] R.M. Sundaram, A. Sekiguchi, M. Sekiya, T. Yamada, K. Hata, Copper/carbon nanotube composites: research trends and outlook, R. Soc. Open Sci. 5 (2018) 180814.

https://doi.org/10.1098/rsos.180814.

[23] A.P. Leggiero, K.J. Trettner, H.L. Ursino, D.J. Mcintyre, M. Schauer, E. Zeira, C.D. Cress, B.J. Landi, High Conductivity Copper–Carbon Nanotube Hybrids via Site-Specific Chemical Vapor Deposition, ACS Appl. Nano Mater. 2 (2018) 118–126. https://doi.org/10.1021/acsanm.8b01740.

[24] R. Sundaram, T. Yamada, K. Hata, A. Sekiguchi, The influence of Cu electrodeposition parameters on fabricating structurally uniform CNT-Cu composite wires, Mater. Today Commun. 13 (2017) 119–125. https://doi.org/10.1016/j.mtcomm.2017.09.003.

[25] M. Ghorbani-Asl, K.Z. Milowska, M. Burda, P.D. Bristowe, K.K.K. Koziol, N. Ćatić, L. Wolanicka, Breaking the electrical barrier between copper and carbon nanotubes, Nanoscale. 9 (2017) 8458–8469. https://doi.org/10.1039/c7nr02142a.

[26] G.J. Wang, Y.J. Ma, Y.P. Cai, Z.H. Cao, X.K. Meng, Overcoming the strength-conductivity trade-off dilemma in carbon nanotube/aluminum-copper fiber by diffusion interface and chemical reaction interface, Carbon N. Y. 146 (2019) 293–300. https://doi.org/10.1016/j.carbon.2019.01.111.

[27] P.M. Hannula, J. Aromaa, B.P. Wilson, D. Janas, K. Koziol, O. Forsén, M. Lundström, Observations of copper deposition on functionalized carbon nanotube films, Electrochim. Acta. 232 (2017) 495–504. https://doi.org/10.1016/j.electacta.2017.03.006.

[28] G.J. Wang, Y.P. Cai, Y.J. Ma, S.C. Tang, J.A. Syed, Z.H. Cao, X.K. Meng, Ultrastrong and Stiff Carbon Nanotube/Aluminum−Copper Nanocomposite via Enhancing Friction between Carbon Nanotubes, Nano Lett. 19 (2019) 6255–6262.

https://pubs.acs.org/doi/abs/10.1021/acs.nanolett.9b02332.

[29] Y. Matsuda, W.Q. Deng, W.A. Goddard, Contact resistance properties between nanotubes and various metals from quantum mechanics, J. Phys. Chem. C. 111 (2007) 11113–11116. https://doi.org/10.1021/jp072794a.

[30] I. Suarez-Martinez, A. Felten, J.J. Pireaux, C. Bittencourt, C.P. Ewels, Transition metal deposition on graphene and carbon nanotubes, J. Nanosci. Nanotechnol. 9 (2009) 6171–6175. https://doi.org/10.1166/jnn.2009.1557.

[31] A. Maiti, A. Ricca, Metal-nanotube interactions - Binding energies and wetting properties, Chem. Phys. Lett. 395 (2004) 7–11. https://doi.org/10.1016/j.cplett.2004.07.024.

[32] D.J. McIntyre, R.K. Hirschman, I. Puchades, B.J. Landi, Enhanced copper – carbon nanotube hybrid conductors with titanium adhesion layer, J. Mater. Sci. (2019). https://doi.org/10.1007/s10853-020-04457-1.

[33] R.G. Charles, M.A. Pawlikowski, Comparative heat stabilities of some metal acetylacetonate chelates, J. Phys. Chem. 62 (1958) 440–444. https://doi.org/10.1021/j150562a017.

[34] J. Von Hoene, R.G. Charles, W.M. Hickam, Thermal decomposition of metal acetylacetonates mass spectrometer studies, J. Phys. Chem. 62 (1958) 1098–1101. https://doi.org/10.1021/j150567a019.

[35] J.R.V. Garcia, T. Goto, Chemical Vapor Deposition of Iridium, Platinum, Rhodium and Palladium, Mater. Trans. 44 (2003) 1717–1728. https://doi.org/10.2320/matertrans.44.1717.

[36] Y. Pauleau, A.Y. Fasasi, Kinetics of Sublimation of Copper(II) Acetylacetonate Complex Used for Chemical Vapor Deposition of Copper Films, Chem. Mater. 3 (1991) 45–50. https://doi.org/10.1021/cm00013a015.

[37] X. Wang, N. Behabtu, C.C. Young, D.E. Tsentalovich, M. Pasquali, J. Kono, High-ampacity power cables of tightly-packed and aligned carbon nanotubes, Adv. Funct. Mater. 24 (2014) 3241–3249. https://doi.org/10.1002/adfm.201303865.

[38] P.G. Collins, K. Bradley, M. Ishigami, A. Zettl, Extreme oxygen sensitivity of electronic properties of carbon nanotubes, Science (80-.). 287 (2000) 1801–1804. https://doi.org/10.1126/science.287.5459.1801.

[39] A. Lekawa-Raus, L. Kurzepa, G. Kozlowski, S.C. Hopkins, M. Wozniak, D. Lukawski, B.A. Glowacki, K.K. Koziol, Influence of atmospheric water vapour on electrical performance of carbon nanotube fibres, Carbon N. Y. 87 (2015) 18–28. https://doi.org/10.1016/j.carbon.2015.02.018.

[40] J.W. Do, D. Estrada, X. Xie, N.N. Chang, J. Mallek, G.S. Girolami, J.A. Rogers, E. Pop, J.W. Lyding, Nanosoldering carbon nanotube junctions by local chemical vapor deposition for improved device performance, Nano Lett. 13 (2013) 5844–5850. https://doi.org/10.1021/nl4026083.

[41] A.R. Bucossi, C.D. Cress, C.M. Schauerman, J.E. Rossi, I. Puchades, B.J. Landi, Enhanced Electrical Conductivity in Extruded Single-Wall Carbon Nanotube Wires from Modified Coagulation Parameters and Mechanical Processing, ACS Appl. Mater. Interfaces. 7 (2015) 27299–27305. https://doi.org/10.1021/acsami.5b08668.

[42] Y. Zhao, J. Wei, R. Vajtai, P.M. Ajayan, E. V Barrera, Iodine doped carbon nanotube cables exceeding specific electrical conductivity of metals, Sci. Rep. 1 (2011) 83. https://doi.org/10.1038/srep00083.

[43] W.M. Haynes, ed., CRC Handbook of Chemistry and Physics (Internet Version 2016), 96th ed., CRC Press/Taylor and Francis, Boca Raton, FL, 2016. http://www.hbcpnetbase.com/ (accessed December 7, 2015).

[44] A.D. Polyanin, A.I. Chernoutsan, A concise handbook of mathematics, physics, and engineering sciences, Taylor & Francis Group, LLC, Boca Raton, FL, 2010. https://doi.org/10.1201/b10276.

[45] T. Weiss, V. Zielasek, M. Bäumer, Influence of Water on Chemical Vapor Deposition of Ni and Co thin films from ethanol solutions of acetylacetonate precursors, Sci. Rep. 5 (2015) 1–13. https://doi.org/10.1038/srep18194.

[46] R. Sundaram, T. Yamada, K. Hata, A. Sekiguchi, The importance of carbon nanotube wire density, structural uniformity, and purity for fabricating homogeneous carbon nanotube-copper wire composites by copper electrodeposition, Jpn. J. Appl. Phys. 57 (2018). https://doi.org/10.7567/JJAP.57.04FP08.

[47] P.M. Hannula, A. Peltonen, J. Aromaa, D. Janas, M. Lundström, B.P. Wilson, K. Koziol, O. Forsén, Carbon nanotube-copper composites by electrodeposition on carbon nanotube fibers, Carbon N. Y. 107 (2016) 281–287. https://doi.org/10.1016/j.carbon.2016.06.008.